CHIN. PHYS. LETT. Vol. 37, No. 11 (2020) 117102 **Express Letter**

Exciton Vortices in Two-Dimensional Hybrid Perovskite Monolayers

Yingda Chen(陈颖达)[1,2], Dong Zhang(张东)[1,2*], and Kai Chang(常凯)[1,2,3*]

[1]*State Key Laboratory for Superlattices and Microstructures, Institute of Semiconductors, Chinese Academy of Sciences, Beijing 100083, China*
[2]*CAS Center for Excellence in Topological Quantum Computation, University of Chinese Academy of Sciences, Beijing 100190, China*
[3]*Beijing Academy of Quantum Information Sciences, Beijing 100193, China*

(Received 2 October 2020; accepted 2 November 2020; published online 8 November 2020)

We study theoretically the exciton Bose–Einstein condensation and exciton vortices in a two-dimensional (2D) perovskite $(PEA)_2PbI_4$ monolayer. Combining the first-principles calculations and the Keldysh model, the exciton binding energy of in a $(PEA)_2PbI_4$ monolayer can approach hundreds of meV, which make it possible to observe the excitonic effect at room temperature. Due to the large exciton binding energy, and hence the high density of excitons, we find that the critical temperature of the exciton condensation could approach the liquid nitrogen regime. In the presence of perpendicular electric fields, the dipole-dipole interaction between excitons is found to drive the condensed excitons confined in $(PEA)_2PbI_4$ monolayer flakes into patterned vortices, as the evolution time of vortex patterns is comparable to the exciton lifetime.

PACS: 71.35.−y, 03.75.Kk, 68.90.+g DOI: 10.1088/0256-307X/37/11/117102

Excitons, the composed bosons formed by bound electron-hole pairs through Coulomb interactions, may collapse into Bose–Einstein condensation (BEC) states at low temperatures.[1−3] Bosons at the BEC regime not only show exotic superfluity,[4] but also possess patterns of vortices.[5,6] Such phenomena have been studied both theoretically and experimentally recently in solids,[7,8] such as two-dimensional transitional metal dichalcogenides.[9] To realize the exciton BEC, one needs to find a system with long exciton lifetime, huge binding energy and small exciton mass. Long exciton radiative lifetime allows the excitons to build up a quasi-equilibrium before recombination, while the huge binding energy leads to small Bohr radius of excitons with high average exciton density. The 2D perovskite monolayers could offer us a possible platform, promising considerably high critical temperature of the exciton BEC.

In the past decades, hybrid organic-inorganic lead halide perovskites have achieved remarkable records in the field of solar cells,[10−13] and shown immense potentials as low-cost alternatives to traditional semiconductors in commercial photovoltaic industry.[14,15] Compared to the three-dimensional (3D) perovskites, 2D layered hybrid perovskites possess superior environment stability in device performances,[16,17] and provide versatile blocks in dimensionality engineering[18,19] of multi-dimensional perovskites due to the structural diversity.[20,21] Surprisingly, the 2D hybrid perovskites display huge exciton binding energies about hundreds of meV[22−24] and long exciton lifetimes about 2.5 ns,[25] even in the presence of high defects and disorders, due to the quantum confinement effects. The two distinguished features make 2D hybrid organic-inorganic lead halide perovskite monolayers the ideal platforms to realize exciton BEC.

In this work, we focus on the typical 2D hybrid perovskite $(PEA)_2PbI_4$.[23,26−28] The $(PEA)_2PbI_4$ possesses a stable layered structure, which comprises alternatively stacked layers of $[PbI_6]^{4-}$ octahedra and long-chain organic molecules $C_6H_5C_2H_4NH_3^+$ (PEA+) as shown in Fig. 1(a). To determine both the crystalline structures and electronic structures, the first-principles calculations are performed using the Vienna *ab initio* simulation package (VASP) within the generalized gradient approximation (GGA) in Perdew–Burke–Ernzerhof (PBE) type and the projector augmented-wave (PAW) pseudopotential. The kinetic energy cutoff is set to 500 eV for wave-function expansion, and the Monkhorst–Pack type k-point grid is sampled by sums over $3\times3\times3$. For the convergence of the electronic self-consistent calculations, the total energy difference criterion is set to 10^{-8} eV. The crystal structure is fully relaxed until the residual forces on atoms are less than 0.01 eV/Å. The spin-orbital coupling effect is taken into consideration, and the van der Waals correction is also included by the DFT-D2

Supported by the National Key R&D Programme of China (Grant Nos. 2017YFA0303400 and 2016YFE0110000), the National Natural Science Foundation of China (Grant Nos. 11574303 and 11504366), the Youth Innovation Promotion Association of Chinese Academy of Sciences (Grant No. 2018148), and the Strategic Priority Research Program of Chinese Academy of Sciences (Grant No. XDB28000000).
*Corresponding authors. Email: zhangdong@semi.ac.cn; kchang@semi.ac.cn
© 2020 Chinese Physical Society and IOP Publishing Ltd

method.

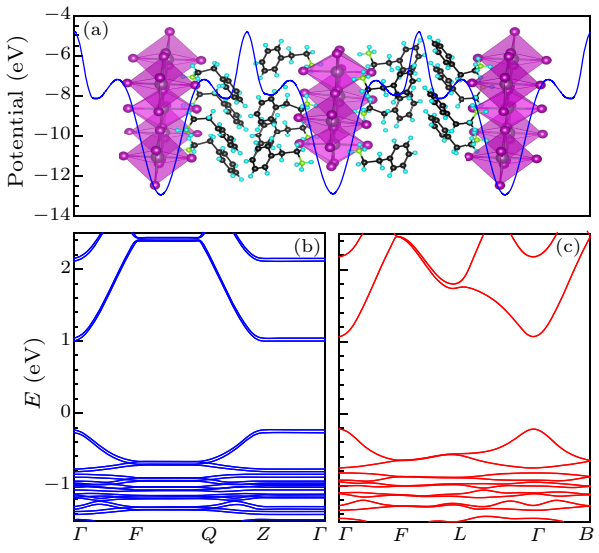

Fig. 1. (a) Schematic of layered hybrid perovskite $(PEA)_2PbI_4$. The different atoms are indicated by different color coding, and the effective inner potential is shown by blue solid lines. The lead, iodide, carbon, hydrogen and nitrogen atoms are displayed by silver, purple, black, cyan and green spheres, respectively. (b) Band structures of bulk $(PEA)_2PbI_4$. (c) Band structures of $(PEA)_2PbI_4$ monolayer.

From Fig. 1(a), one can see that the inorganic layers of PbI_4 are sandwiched between two organic layers, with the effective potential barriers as high as 8.1 eV, as illustrated by the blue solid curves. Such high potential barriers make $(PEA)_2PbI_4$ behaves like stacking quantum wells with hard-wall confining potentials. Due to the weak interlayer van der Waals coupling, we find that the electronic structures are similar between the bulk material [see Fig. 1(b)] and its monolayer [see Fig. 1(c)]. The band structures are all over high symmetric reciprocal points in the Brillouin zone. The parabolic conduction and valence bands are isolated with bulk bands, and possess a direct band gap estimated to be 1.24 eV. The direct band gap feature ensures good performance of $(PEA)_2PbI_4$ in optoelectronic devices. Notice that the band structures of the $(PEA)_2PbI_4$ monolayer [see Fig. 1(c)] possess a direct band gap about 1.278 eV at the Γ point. Unlike other 2D materials whose band gap vary significantly as the thickness decreases to monolayer, e.g., the black phosphorous. The dimensionality reduction from bulk to the monolayer limit does not increase the band gap evidently, since the individual monolayer is naturally well confined by the internal potential barriers, and the interlayer van der Waals coupling is quite weak.

Based on the band structures obtained from the first-principles calculations, we study the excitons in $(PEA)_2PbI_4$ monolayer. The internal motion of exciton is governed by

$$\Big[-\frac{\hbar^2}{2\mu}\nabla_{\boldsymbol{\rho}}^2 + V_{2D}(\boldsymbol{\rho})\Big]\psi = \mathcal{E}\psi. \quad (1)$$

where $\boldsymbol{\rho} = (\rho, \varphi)$ is the relative displacement between the electron and hole, the reduced mass $\mu = m_e m_h/(m_e + m_h)$, the electron mass $m_e = 0.208m_0$, and the hole mass $m_h = 0.372m_0$. The electron mass and hole mass are adopted from the first-principles calculated band dispersions along Γ–L path in k-space, respectively. Considering the ultrathin thickness of the $(PEA)_2PbI_4$ monolayer, the Keldysh potential[29] can be used to describe the Coulomb interaction between the electron and hole as follows:

$$V_{2D}(\rho) = -\frac{e^2}{4\pi\epsilon_0\epsilon_2\rho_0}\frac{\pi}{2}\Big[H_0\Big(\frac{\rho}{\rho_0}\Big) - Y_0\Big(\frac{\rho}{\rho_0}\Big)\Big], \quad (2)$$

where the screening length of the PbI_4 layer $\rho_0 = r_0/\epsilon_2$, and $r_0 = \epsilon_1 L_w(1 + \epsilon_2/\epsilon_1^2)/2$. The relevant parameters in the Keldysh potential are defined as follows. For the sandwiched inorganic PbI_4 layer, the width $L_w = 6.36$ Å,[23] and the relative permittivity $\epsilon_1 = 6.10$.[22,23] For the organic barriers, the width $L_b = 9.82$ Å, and the relative permittivity $\epsilon_2 = 3.32$.[23] The exciton binding energy $\mathcal{E}_b$ can be obtained by applying the variational method to Eq. (1). With the parameters given above, the exciton binding energy is about $\mathcal{E}_b = 238.5$ meV, which agrees well with the experimental result 220–250 meV.[23,30] Correspondingly, the exciton spectrum of the $(PEA)_2PbI_4$ monolayer (the red solid lines) calculated from Eq. (1) is shown in Fig. 2(a). The PL maximum $E_0 = E_g - \mathcal{E}_b \simeq 2.34$ eV is close to the experimental value 2.4 eV[23] and 2.37 eV,[27] when the bandgap takes the experimental value $E_g = 2.58$ eV as reported in Ref. [23].

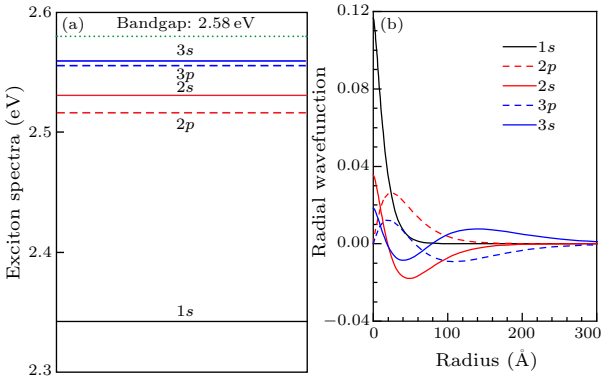

Fig. 2. (a) Exciton spectrum in perovskite monolayer estimated by the Keldysh model. The solid lines show the s states, while the dashed lines show the p states. The dotted green line gives the free carrier limit, which is determined by the bandgap of the 2D perovskite. (b) The schematic of radial distribution of exciton wavefunctions.

When a perpendicular electric field is applied, the effective electron-hole interaction becomes dependent on the z-directional distribution of the electron (z_e) and hole (z_h). The Keldysh potential takes the form

[generalized from Eq. (2)]

$$V(\rho, z_{\rm e}, z_{\rm h}) = -\frac{e^2}{4\pi\epsilon_0\rho}\int_0^\infty \frac{J_0(t)}{\epsilon^{\rm 2D}_{\rm mac}(t/\rho, z_{\rm e}, z_{\rm h})}dt, \quad (3)$$

where the dielectric function is expressed as

$$\epsilon^{\rm 2D}_{\rm mac} \simeq e^{q|z_{\rm e}-z_{\rm h}|}\Big[\epsilon_2 + L_{\rm w}q\frac{\epsilon_1}{2}\Big(1+\frac{\epsilon_2^2}{\epsilon_1^2}\Big)\Big] \quad (4)$$

in the thin film limit. By expanding the equation of exciton motion, i.e., Eq. (1), into three dimensional (3D) form, the exciton motions under the electric field are obtained,

$$\Big[-\frac{\hbar^2}{2\mu}\nabla^2_{\boldsymbol{\rho}} - \frac{\hbar^2}{2M}\nabla^2_{\boldsymbol{R}} + H_{\rm ez}(z_{\rm e}) + H_{\rm hz}(z_{\rm h}) + V\Big(\rho, z_{\rm e}, z_{\rm h}\Big)\Big]\psi = \mathcal{E}\psi. \quad (5)$$

Here $\boldsymbol{R}$ represents the displacement of the center of mass (c.m.) of the exciton, $M = m_{\rm e} + m_{\rm h}$ is the c.m. mass of the exciton. $H_{\rm ez}(H_{\rm hz})$ denotes the single-particle Hamiltonian of the electron (hole) in the inorganic layer under the external electric field F. Variational exciton wavefunction,[31] associated with the $l_{\rm h}$th electron and $l_{\rm e}$th hole subbands, i.e.,

$$\psi^{l_{\rm e}l_{\rm h}}_{nm}(\rho, z_{\rm e}, z_{\rm h}) = N^{l_{\rm e}l_{\rm h}}\zeta_{l_{\rm e}}(z_{\rm e})\zeta_{l_{\rm h}}(z_{\rm h})e^{-\sqrt{(\frac{z_{\rm e}-z_{\rm h}}{z_0})^2+(\frac{\rho}{a_0})^2}}, \quad (6)$$

is adopted for the 1s-type state in Eq. (5), with variational parameters a_0 and z_0. The z-directional confinements of the electron and hole are included in $\zeta_{l_{\rm e}}$ and $\zeta_{l_{\rm h}}$ (see Section S1 in the Supplementary Materials).

For the 1s-type exciton state, the effects of perpendicular electric fields are limited. As shown in Fig. 3(a), the band gap of the perovskite monolayer remains unchanged under an electric field 2 MV/cm. Accordingly, the binding energy of the exciton varies slightly. From Fig. 3(b), one can find that the binding energy drops merely 0.06 meV as the strength of the perpendicular electric field increases up to a very strong electric field 20 MV/cm. The reason lies in the fact that it is difficult to separate electrons and holes vertically, as shown in Fig. 3(c), in the presence of perpendicular electric field as strong as 20 MV/cm, the effective spatial separation between centers of holes and electrons d along the z-axis is less than 1 Å. This feature arises from the very strong confining potential (about 8 eV) and weak inter-layer coupling.

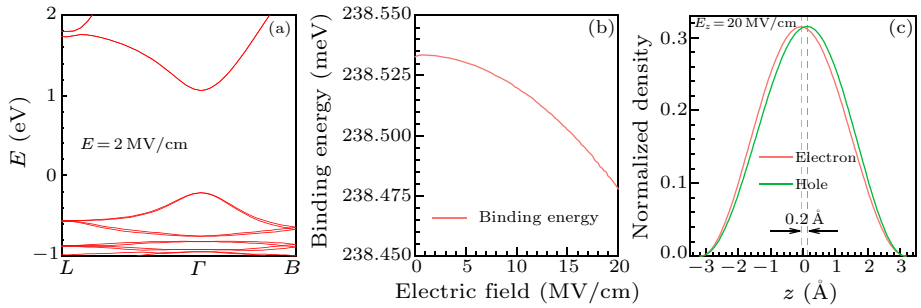

Fig. 3. (a) Band structures of $(PEA)_2PbI_4$ monolayers under external electric field of 2 MV/cm. (b) The exciton binding energies and strengths of perpendicular electric fields. (c) The electron-hole spatial separation as a function of perpendicular electric field. The effective separation is denoted by distance between centers of electrons (red lines) and holes (green lines).

Although perpendicular electric field changes extremely slightly the binding energies and Bohr radius of the perovskite monolayer, it is efficient to align dipoles, change the exciton-exciton interactions utterly, and play a crucial role in the exciton BEC under the critical temperature.

The critical temperature for the BEC transition in the flakes of $(PEA)_2PbI_4$ monolayer is estimated by

$$T_{\rm c} = \frac{\pi\hbar^2 n}{Mk_{\rm B}}\frac{1}{\ln(nS/2)}, \quad (7)$$

where S is the area of the flake, and n is the exciton density. For a square flake, with $S = 20^2\,{\rm nm}^2$ and $n = 5\times10^{12}\,{\rm cm}^{-2}$, we obtain $T_{\rm c} \simeq 106\,{\rm K}$. Therefore, the exciton condensation can be achieved at the temperature under liquid nitrogen regime in $(PEA)_2PbI_4$ monolayer.

Usually, the Gross–Pitaevskii (GP) equation is widely used to describe the condensate states. Considering laser pumping and exciton recombination process, the non-equilibrium exciton condensates in the perovskite monolayer with the lateral boundaries can be described by the complex Gross–Pitaevskii (cGP) equation in the mean-field approach. Under a weak perpendicular electric field, the exciton-exciton interaction is dominated by repulsive dipole-dipole interaction (DDI), which can be expressed as $V_{\rm dd}$ in reciprocal space,

$$V_{\rm dd}(\boldsymbol{Q}) = \frac{e^2 d}{\epsilon_0\epsilon_1}\frac{2[(1+\frac{\epsilon_2}{\epsilon_1})e^{x_Q} + (1-\frac{\epsilon_2}{\epsilon_1})e^{-x_Q}] - 4}{x_Q[(1+\frac{\epsilon_2}{\epsilon_1})^2e^{x_Q} - (1-\frac{\epsilon_2}{\epsilon_1})^2e^{-x_Q}]}, \quad (8)$$

with $x_Q = Qd$. Here d is the electron-hole separation introduced by the electric field. Thus the cGP equation is expressed as

$$i\hbar\partial_t\psi = \Big[-\frac{\hbar^2}{2M}\nabla^2_{\boldsymbol{R}} + V_{\rm c} + H_{\rm dd} + i\hbar\Big(\hat{R} - \Gamma|\psi|^2\Big)\Big]\psi, \tag{9}$$

where $\hat{R}$ is the pumping rate, $\Gamma = 1/2\tau_{\rm ex}$ the recombination rate, and $\tau_{\rm ex}$ the exciton lifetime. $V_{\rm c}$ denotes the trap potential for excitons. It is worth noting that convolution of $H_{\rm dd} = V_{\rm dd} * |\psi|^2$ stands for the DDI, which displays a nonlinear behavior.

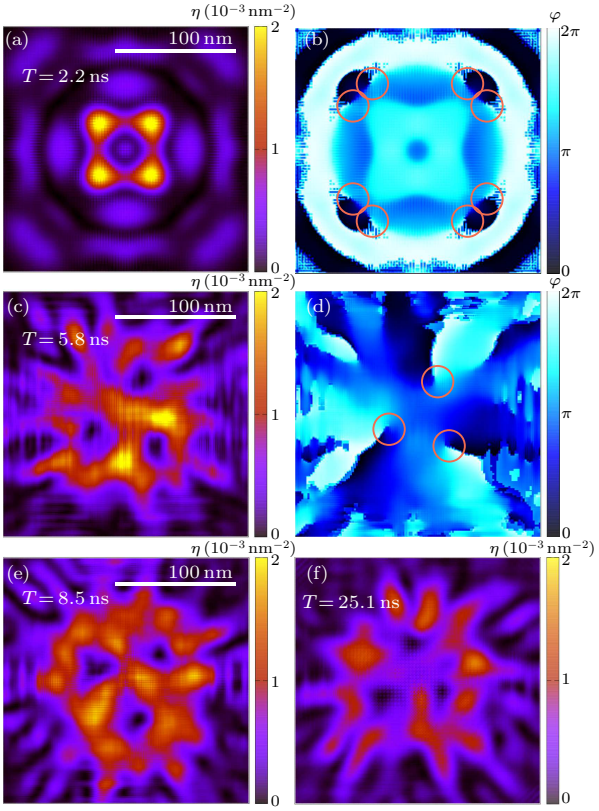

Fig. 4. Dynamic evolution of exciton vortices patterns in perovskite monolayer flake. (a) Contour map of the density of the exciton condensate wavefunction, at the first occurrence of occasional exciton vortices pattern. (b) The phase distributions of the exciton condensate wavefunction. (c) and (d) Density and phase distributions of exciton condensate wavefunction of the stable vortex patterns. (e) and (f) Density of exciton condensate wavefunction of the stable vortex patterns at $T = 8.5$ ns and $T = 25.1$ ns, respectively. The density $\eta = |\psi|^2$ is in units of $10^{-3}\,\mathrm{nm}^{-2}$. The orange circles show the locations of the vortices.

Considering that the laser pumping is generally radial symmetric, while the perovskite flakes possess irregular shapes in practice, the disorders induced by the lateral boundary provide the scattering to the optically generated excitons, and change the directions of their momentum. As a consequence, non-zero angular velocities appear at the edges of the flakes. In the presence of the nonlinear DDI term of the flake boundaries, the exciton condensate state is sensitive to the local angular velocities raised by the lateral disorders, which behave as local potentials surrounding the condensate cloud. Therefore, the exciton vortices are expected to emerge in the perovskite monolayer flakes with constant laser pumping.

In order to demonstrate the vortex states, the complex GP equation (9) is solved by time-splitting spectral methods in combination with discrete sine transforms.[32–35] The pumping and decaying process in each time step is shown in Section S2 in the Supplementary Materials. The parameters for exciton vortex simulations in a square flake of $(PEA)_2PbI_4$ monolayer with length $L_0 = 400$ nm are listed as follows. The flake is sampled by a 512×512 mesh in real space, and the time step is set to be 5×10^{-6} ns, to reach high accuracy. The pump power is set to be $\hat{R} \simeq 2 \times 10^{-3}$ meV, and the exciton lifetime is $\tau_{\rm ex} = 2$ ns. A shallow harmonic potential is also introduced to mimic interface potential fluctuations in the quantum well structures, i.e., we set $V_{\rm c} = V_0 R^2/2L_0^2$ for $|R_x|, |R_y| < L_0$ and $V_{\rm c} = \infty$ for the rest R_x, R_y, with $V_0 \sim 10$ meV and $R = \sqrt{R_x^2 + R_y^2}$.

The simulated exciton vortices are shown in Fig. 4. The vortex is characterized by a rotation of phase of the condensate wavefunction around the singular point by an integer multiple of 2π. As shown in Fig 4(a), the first occasional vortices emerge during the dynamic evolution of the exciton condensates at $T = 2.2$ ns. The eight vortices locate at the dark spots in the contour plot of the density of the exciton condensate wavefunction. The corresponding phase distributions in Fig. 4(b), indicate 2π phase shift around the singular points of the wavefunction, which indicates the existence of exciton vortices. As time goes by, the vortex patterns tend to reach dynamic equilibrium since $T = 5.8$ ns. From Figs. 4(c) and 4(d), one can find that there are three vortices in the central area of the perovskite monolayer flake. The three vortices are stable and rotating persistently, as illustrated at $T = 8.5$ ns, and even $T = 25.1$ ns, respectively, as shown in Figs. 4(e) and 4(f). Since the evolution time of vortices patterns is comparable to the exciton lifetime, it is promising to observe exciton vortex patterns in $(PEA)_2PbI_4$ monolayers experimentally.

In summary, we have studied the exciton BEC and its vortices in $(PEA)_2PbI_4$ monolayer, and calculated exciton binding energy 238.5 meV is in good agreement with experimental results. It is found that the perpendicular electric fields can change slightly the binding energy and Bohr radius in $(PEA)_2PbI_4$ monolayer, while they are efficient to align the electron-hole dipoles. With laser pumping, the repulsive dipole-dipole interaction created by the perpendicular electric field can drive the laterally confined excitons into various vortex patterns. The evolution time of those vortices is comparable to the exciton lifetime, and reach a stable pattern with certain number of vortices

rotating at the center. Since the large exciton binding energy ensures the critical temperature of the exciton BEC within the liquid nitrogen regime, it is possible to realize stable exciton vortices in two-dimensional hybrid perovskite monolayers.

References

[1] Snoke D W, Wolfe J P and Mysyrowicz A 1990 *Phys. Rev. Lett.* **64** 2543
[2] Butov L V, Lai C W, Ivanov A L, Gossard A C and Chemla D S 2002 *Nature* **417** 47
[3] Butov L V, Zrenner A, Abstreiter G, Bohm G and Weimann G 1994 *Phys. Rev. Lett.* **73** 304
[4] Rayfield G W and Reif F 1964 *Phys. Rev.* **136** A1194
[5] Yarmchuk E J, Gordon M J V and Packard R E 1979 *Phys. Rev. Lett.* **43** 214
[6] Keeling J and Berloff N G 2008 *Phys. Rev. Lett.* **100** 250401
[7] Lagoudakis K G, Ostatnicky T, Kavokin A V, Rubo Y G, André R and Deveaud-Plédran B 2009 *Science* **326** 974
[8] Roy I, Dutta S, Choudhury A N R, Basistha S, Maccari I, Mandal S, Jesudasan J, Bagwe V, Castellani C, Benfatto L and Raychaudhuri P 2019 *Phys. Rev. Lett.* **122** 047001
[9] Chen Y D, Huang Y W, Lou W K, Cai Y Y and Chang K 2020 *Phys. Rev. B* **102** 165413
[10] Kojima A, Teshima K, Shirai Y and Miyasaka T 2009 *J. Am. Chem. Soc.* **131** 6050
[11] You J, Dou L, Yoshimura K, Kato T, Ohya K, Moriarty T, Emery K, Chen C C, Gao J, Li G and Yang Y 2013 *Nat. Commun.* **4** 1446
[12] Zhou H, Chen Q, Li G, Luo S, Song T B, Duan H S, Hong Z, You J, Liu Y and Yang Y 2014 *Science* **345** 542
[13] Zhao W Y, Ku Z L, Lv L P, Lin X, Peng Y, Jin Z M, Ma G H and Yao J Q 2019 *Chin. Phys. Lett.* **36** 028401
[14] Jena A K, Kulkarni A and Miyasaka T 2019 *Chem. Rev.* **119** 3036
[15] Nayak P K, Mahesh S, Snaith H J and Cahen D 2019 *Nat. Rev. Mater.* **4** 269
[16] Tennyson E M, Doherty T A S and Stranks S D 2019 *Nat. Rev. Mater.* **4** 573
[17] Xie W R, Liu B, Tao T, Zhang G G, Zhang B H, Xie Z L, Chen P, Chen D J and Zhang R 2017 *Chin. Phys. Lett.* **34** 068103
[18] Grancini G and Nazeeruddin M K 2019 *Nat. Rev. Mater.* **4** 4
[19] Quan L N, Yuan M, Comin R, Voznyy O, Beauregard E M, Hoogland S, Buin A, Kirmani A R, Zhao K, Amassian A, Kim D H and Sargent E H 2016 *J. Am. Chem. Soc.* **138** 2649
[20] Li Z, Klein T R, Kim D H, Yang M, Berry J J, van Hest M F A M and Zhu K 2018 *Nat. Rev. Mater.* **3** 18017
[21] Lee M M, Teuscher J, Miyasaka T, Murakami T N and Snaith H J 2012 *Science* **338** 643
[22] Ishihara T, Takahashi J and Goto T 1990 *Phys. Rev. B* **42** 11099
[23] Hong X, Ishihara T and Nurmikko A V 1992 *Phys. Rev. B* **45** 6961
[24] Yaffe O, Chernikov A, Norman Z M, Zhong Y, thapillai A V, van der Zande A, Owen J S and Heinz T F 2015 *Phys. Rev. B* **92** 045414
[25] Fang H H, Yang J, Adjokatse S, Tekelenburg E, minga M E K, Duim H, Ye J, Blake G R, Even J and Loi M A 2020 *Adv. Funct. Mater.* **30** 1907979
[26] Smith M D, Connor B A and Karunadasa H I 2019 *Chem. Rev.* **119** 3104
[27] Du K Z, Tu Q, Zhang X, Han Q, Liu J, Zauscher S and Mitzi D B 2017 *Inorg. Chem.* **56** 9291
[28] Do T T H, Aguila A G D, Zhang D, Xing J, Liu S, Prosnikov M A, Gao W, Chang K, Christianen P C M and Xiong Q 2020 *Nano Lett.* **20** 5141
[29] Keldysh L V 1979 *Sov. Phys.-JETP* **29** 658
[30] Cheng B, Li T Y, Maity P, Wei P C, Nordlund D, Ho K T, Lien D H, Lin C H, Liang R Z, Miao X, Ajia I A, Yin J, Sokaras D, Javey A, Roqan I S, Mohammed O F and He J H 2018 *Commun. Phys.* **1** 80
[31] Miller D A B, Chemla D S, Damen T C, Gossard A C, Wiegmann W, Wood T H and Burrus C A 1985 *Phys. Rev. B* **32** 1043
[32] Bao W and Cai Y 2015 *SIAM J. Appl. Math.* **75** 492
[33] Bao W and Cai Y 2013 *Kinet. & Relat. Models* **6** 1
[34] Bao W and Cai Y 2018 *Commun. Comput. Phys.* **24** 899
[35] Sierra J, Kasimov A, Markowich P and Weishäupl R M 2015 *J. Nonlinear Sci.* **25** 709

Supplementary Materials for Exciton vortices in two-dimensional hybrid perovskite monolayers

Yingda Chen and Dong Zhang*
SKLSM, Institute of Semiconductors, Chinese Academy of Sciences, P.O. Box 912, Beijing 100083, China and CAS Center for Excellence in Topological Quantum Computation, University of Chinese Academy of Sciences, Beijing 100190, China

Kai Chang†
SKLSM, Institute of Semiconductors, Chinese Academy of Sciences, P.O. Box 912, Beijing 100083, China CAS Center for Excellence in Topological Quantum Computation, University of Chinese Academy of Sciences, Beijing 100190, China and Beijing Academy of Quantum Information Sciences, Beijing 100193, China

SECTION S1: SOLUTION OF THE QUANTUM CONFINED EXCITON UNDER ELECTRIC FIELD

The single particle $H_{ez}(H_{hz})$ denotes the Hamiltonian of the electron(hole) in the inorganic layer under the electric field F, i.e.,

$$\begin{cases} H_{ez}(z_e) = -\frac{\hbar^2}{2m_e}\frac{\partial^2}{\partial z_e^2} + V_{\text{conf}}(z_e) + eFz_e \\ H_{hz}(z_h) = -\frac{\hbar^2}{2m_h}\frac{\partial^2}{\partial z_h^2} + V_{\text{conf}}(z_h) - eFz_h \end{cases}, \tag{S1}$$

where V_{conf} is the infinite-potential-barrier for the electron and the hole, since they are confined in the single inorganic layer. Eigenstates of Eq.(S1) are represented by the Airy functions Ai and Bi,

$$\zeta_{l_e(l_h)}(z) = a_{l_e(l_h)}\text{Ai}\left(Z_{l_e(l_h)}(z)\right) + b_{l_e(l_h)}\text{Bi}\left(Z_{l_e(l_h)}(z)\right), \tag{S2}$$

where $l_e(l_h) = 1, 2, \ldots$ is the subband index of the electron(hole), and

$$\begin{cases} Z_{l_e} = -[2m_e/(e\hbar F)^2]^{\frac{1}{3}}(E_{l_e}^{(e)} - eFz) \\ Z_{l_h} = -[2m_h/(e\hbar F)^2]^{\frac{1}{3}}(E_{l_h}^{(h)} + eFz) \end{cases}. \tag{S3}$$

Here $E_{l_e}^{(e)}(E_{l_h}^{(h)})$ is the l_e-th electron (l_h-th hole) subband energy. The parameters are normalized as

$$\begin{cases} a_l = [1 + \text{Ai}^2(Z_{l\pm})/\text{Bi}^2(Z_{l\pm})]^{-1/2} \\ b_l = -a_l\text{Ai}(Z_{l\pm})/\text{Bi}(Z_{l\pm}) \end{cases} \tag{S4}$$

, with $Z_{l\pm} = Z_l(z = \pm L_w/2)$. The eigenenergies E_l are determined by the $(l-1)$-zeros of

$$S(E_l) = \text{Ai}(Z_{l+})\text{Bi}(Z_{l-}) - \text{Bi}(Z_{l+})\text{Ai}(Z_{l-}). \tag{S5}$$

SECTION S2: TREATMENT OF THE PUMPING AND DECAYING TERM

Here we deal with the time step containing the pumping and decaying term $i\partial_t\psi = i\left(\hat{R} - \Gamma|\psi|^2\right)\psi$, which can be written as

$$\partial_t\psi = \left(\hat{R} - \Gamma|\psi|^2\right)\psi. \tag{S6}$$

Since the Eq.(S6) is real, we have

$$\partial_t\rho = 2\left(\hat{R} - \Gamma\rho\right)\rho. \tag{S7}$$

Next we solve $\rho(t)$ from Eq.(S7), and obtain

$$\rho(t) = \frac{\hat{R}}{\Gamma}\frac{1}{1 + Ce^{-2\hat{R}t}}, \tag{S8}$$

with

$$C = \frac{\hat{R}}{\Gamma}\frac{1}{\rho_0} - 1. \tag{S9}$$

Recalling Eq.(S6),

$$\psi_1' = e^{\int_0^{\Delta t}(\hat{R}-\Gamma\rho(s))ds}\psi_1, \rho(0) = \psi_1^2. \tag{S10}$$

Putting Eq.(S8) into the integral in Eq.(S10), we have

$$\int_0^{\Delta t}\left(\hat{R} - \Gamma\rho(s)\right)ds = \hat{R}\Delta t + \frac{1}{2}\ln\left(\frac{\hat{R}}{\hat{R} + \Gamma\rho_0\left(e^{2\hat{R}\Delta t} - 1\right)}\right) \tag{S11}$$

The second-order time splitting can be written as

$$\psi(t + \Delta t) = e^{-i\frac{T}{2}\Delta t}e^{-i\frac{V}{2}\Delta t}e^{\int_0^{\Delta t}(\hat{R}-\Gamma\rho(s))ds}e^{-i\frac{V}{2}\Delta t}e^{-i\frac{T}{2}\Delta t}\psi(t). \tag{S12}$$

* zhangdong@semi.ac.cn
† kchang@semi.ac.cn